Many-body theory of hyperfine interaction in the manganese atom including relativistic effects*

J. Andriessen

Laboratorium voor Technische Natuurkunde, Technische Hoge School, Delft, Netherlands

S. N. Ray, Taesul Lee,[†] and T. P. Das

Department of Physics, State University of New York, Albany, New York 12222

D. Ikenberry

California State College, San Bernadino, California 92407

Using the linked-cluster many-body perturbation procedure we have evaluated the magnetic hyperfine constant A in the spin-Hamiltonian term $A\vec{I}\cdot\vec{J}$ of manganese atom. The nonrelativistic value of A is found to be -90.8 ± 3.0 MHz, composed of -152.6 MHz from the exchange core polarization (ECP) effect and 61.8 MHz from a combination of consistency and correlation effects. We have also made a relativistic calculation of the ECP effect and used this to make estimates of the relativistic effects on $(1,1)$ and $(0,2)$ diagrams. On combining these relativistic results with those from nonrelativistic theory and including the calculated Casimir contribution of -4.3 MHz discussed by Sandars and Beck, our net theoretical value for the hyperfine constant A turns out to be -74.1 ± 3.0 MHz, which is in the good agreement with the experimental results of -72.422 ± 0.002 MHz. Physical explanations are discussed for the trends of the contributions from various effects and their variations from shell to shell.

I. INTRODUCTION

Theoretical studies of the hyperfine interaction in transition-metal and rare-earth atoms, including many-body effects, are important for several reasons. The most important of these is that in contrast to the transition-metal ions where hyperfine data are available only in the solid state, the experimental data for the atoms are available in the free state via several techniques, including atomic-beam and optical-pumping methods.[1] One can therefore carry out a comparison between theoretical and experimental results without having to deal with the question of the influence of the environment (such as covalency effects) which comes up in the case of ions.

In the present work we shall be concerned with the manganese atom, which is particularly convenient to handle because it has a spherically symmetric half-filled 3d shell. Additionally, it has a loosely bound 4s shell which is substantially spin polarized by its exchange interaction with the 3d electrons, its contribution to the hyperfine constant being opposite in sign and comparable in magnitude to the net contribution from the core s states.

Correlation effects in this atom are expected to be particularly important for two reasons. First, because of the cancellation effect between the spin-polarization contributions from the 4s shell and core s shells, the net spin-polarization contribution is reduced, in contrast to the situation in transition-metal ions where the 4s shell is absent,[2]

making the correlation effects more significant. Second, since the 4s shell is relatively loosely bound, its spatial character is expected to be substantially affected by correlation effects which would lead to corresponding changes in the hyperfine constant. Another important reason for studying the Mn atom carefully is that it affords a good opportunity to study the role of relativistic effects. The atom is large enough for one to expect significant contributions from relativistic effects, while at the same time it is not too complicated to make quantitative relativistic analysis impossible. It will be shown later in this paper, using the results of a relativistic treatment of exchange-core-polarization effects, that relativistic effects do not always lead to a straightforward enhancement over nonrelativistic contributions, as might be expected from relativistic hyperfine studies in hydrogen and alkali atoms.[3,4]

It is evident that for a complete understanding of the hyperfine interaction in transition-metal atoms a complete relativistic many-body–theory treatment is necessary. Such an investigation, which can in principle be carried out by an extension of the linked-cluster many-body perturbation theory (LCMBPT) used in nonrelativistic treatments,[5] is expected to be rather complicated and time-consuming. The present work is a prelude or first step towards the understanding of the influence of relativistic effects on spin-polarization, consistency, and correlation contributions to the hyperfine constant. We have carried out both a full nonrelativistic LCMBPT treatment of the hyperfine

interaction in the Mn^0 atom and a relativistic LCMBPT treatment of exchange-core-polarization contributions. From the latter, inferences have been drawn regarding the influence of relativistic effects on the core and valence orbitals and on their mutual interaction, and estimates have been made of relativistic corrections to the important consistency and correlation diagrams of LCMBPT theory.

In Sec. II we give a brief description of the non-relativistic LCMBPT procedure for the Mn^0 atom, with an explanation of the various diagrams. Section III deals with the nonrelativistic results for various orders of perturbation due to electron-electron interaction. The description of the relativistic LCMBPT procedure used to evaluate exchange-core-polarization diagrams and their contributions have been given in Sec. IV. Section V contains a discussion of our results, including relativistic effects and comparison with experiment.

II. DESCRIPTION OF NONRELATIVISTIC LCMBPT PROCEDURE FOR THE MANGANESE ATOM

A. LCMBPT formalism

Since the details of the LCMBPT procedure have been discussed in earlier literature,[4] we give here only a brief description of the procedure and pertinent diagrams for the manganese atom. The exact nonrelativistic Hamiltonian for the N-electron atom can be written as

$$\mathcal{3C} = \sum_{i=1}^{N} T_i + \sum_{i>j}^{N} v_{ij}, \tag{1}$$

where T_i is the kinetic energy plus the nuclear Coulomb operator for the ith electron and v_{ij} is the Coulomb interaction between the ith and jth electrons. One needs the exact solution of the Schrödinger equation

$$\mathcal{3C}\Psi = E\Psi. \tag{2}$$

The exact solution of Eq. (2) is not possible; thus we choose a convenient zero-order one-electron Hamiltonian $\mathcal{3C}_0$, defined by

$$\mathcal{3C}_0 = \sum_{i=1}^{N} (T_i + V_i), \tag{3}$$

which can be solved exactly, and treat the difference

$$\mathcal{3C}' = \mathcal{3C} - \mathcal{3C}_0 = \sum_{i>j} v_{ij} - \sum_i V_i \tag{4}$$

as a perturbation. For our work, we shall choose, as usual, for the V_i the V^{N-1} potential for the Mn^0 atom in the restricted Hartree-Fock (RHF) scheme.[5] The diagrams in various orders incor-

porate, as usual, the features of exchange-core-polarization (unrestricted Hartree-Fock approximation) and correlation effects. The zero-order wave function is the eigenfunction of $\mathcal{3C}_0$, namely, the determinant Φ_0 composed of the N lowest-energy solutions ϕ_n of the single-particle equations

$$(T + V)\phi_n = \epsilon_n \phi_n. \tag{5}$$

The linked-cluster expansion[6] allows one to write the exact eigenfunction Ψ of $\mathcal{3C}$ in the form

$$\Psi_L = \sum_{n=0}^{\infty} {}_L \left(\frac{\mathcal{3C}'}{E_0 - \mathcal{3C}_0}\right)^n \Phi_0, \tag{6}$$

where L indicates that only linked terms in the wave functions are to be retained in the corresponding diagrams. With this wave function Ψ_L one can write the expectation value of the operator O as

$$\langle O \rangle = \sum_{m=0}^{\infty} \sum_{n=0}^{\infty} \langle \Phi_0 | \left(\frac{\mathcal{3C}'}{E_0 - \mathcal{3C}_0}\right)^m O \left(\frac{\mathcal{3C}'}{E_0 - \mathcal{3C}_0}\right)^n | \Phi_0 \rangle_L, \tag{7}$$

L indicating here retention only of linked expectation-value diagrams. In Eq. (7), m and n represent the orders of perturbation. In LCMBPT literature,[5] the diagrams are grouped together according to definite values of m and n and these are referred to as (m,n) diagrams.

The contact Hamiltonian $\mathcal{3C}_c$, which represents the hyperfine effect of interest in the present work, is given by

$$\mathcal{3C}_c = \frac{8\pi}{3} \frac{\mu_e \mu_N}{I a_B^3} \vec{I} \cdot \sum_{i=1}^{N} 2\vec{s}_i \delta(\vec{r}_i), \tag{8}$$

whereas for the experimental determination of hyperfine structure one uses the spin Hamiltonian

$$\mathcal{3C}_{spin} = A_c \vec{I} \cdot \vec{J}. \tag{9}$$

In Eq. (9) A_c is the contact hyperfine-coupling constant. Comparing Eqs. (8) and (9) one can thus write A_c in MHz as

$$A_c = 10^{-6} \frac{8\pi}{3} \left(\frac{\mu_e \mu_N}{I M_J a_B^3 h}\right)$$

$$\times \langle \Psi(J, M_J) | \sum_{i=1}^{N} 2s_{z_i} \delta(\vec{r}_i) | \Psi(J, M_J) \rangle. \tag{10}$$

In general, the hyperfine constant in Eq. (9) can involve contributions for dipolar and orbital hyperfine terms in the Hamiltonian, in addition to A_c. In nonrelativistic theory, due to the fact that the Mn atom is spherical in the ground state the other contributions besides A_c vanish. Equation (10) can be rewritten in the form

$$A_c = K_c D, \tag{11}$$

where

$$K_c = \frac{8\pi}{3} \frac{\mu_e \mu_N}{IJa_B^3 h} 10^{-6} \text{ MHz} = 221.3246 \text{ MHz}, \quad (12)$$

using the tabulated values[7] of μ_e, a_B, h, the nuclear magnetic moment μ_N of ^{55}Mn, $I = \frac{5}{2}$ and $J = \frac{5}{2}$, and

$$D = \left\langle \Psi(J,J) \middle| \sum_{i=1}^{N} 2s_{z_i} \delta(\vec{r}_i) \middle| \Psi(J,J) \right\rangle \quad (13a)$$

is the nonrelativistic spin density in units of a_B^{-3}. In evaluating D through the perturbation diagrams of many-body perturbation theory, we make use of Eq. (7) with O given by the spin-density operator

$$\sum_{i=1}^{N} 2s_{z_i} \delta(\vec{r}_i).$$

The nonrelativistic one-electron spin density between states n and n' is given by the expression

$$\rho^{NR} = \langle \phi_n | \delta(\vec{r}) | \phi_{n'} \rangle. \quad (13b)$$

B. Choice of basic states

The one-electron potential V in Eq. (5) depends on our choice of zero-order Hamiltonian; as mentioned before, we have used for V a V^{N-1} potential. There is no unique way of choosing the zero-order V^{N-1} potential and a judicious decision has to be made for it, keeping in mind various considerations such as the nature of the operator used in Eq. (7) and the type of correlation that is important for the property concerned. With this in mind, we have obtained the excited s states in the $4s$ potential. For the p states we have generated two sets of basic states, one in the $3p$ potential and the other in the $4s$ potential. The motivation for obtaining two such sets was twofold. One was to see how the net result depended on two different choices of basis sets and the other was to determine at least the $4p$ state in the $4s$ potential because the $4s \rightarrow 4p$ excitation is very important for correlation effects of $4s$. It was observed that the difference between the net results of A_c determined with two different potentials was only 1 MHz, which is proportionately very small compared to the experimental value. Thus the final results have the satisfactory feature of not being dependent on the choice of the V^{N-1} potential, although the individual diagrams understandably differ for the two choices. Thus the energy difference ϵ_{4p} − ϵ_{4s}, when the $4p$ state was generated in the $3p$ potential, was found to be 0.01 a.u., whereas it was equal to 0.11 a.u. when the $4p$ state was generated in the $4s$ potential. This latter value is comparable with the experimental energy difference of 0.22 a.u. between the ground $(3d^5 4s^2; {}^6S)$ and excited $(3d^4 4s 4p; {}^6D)$ states of the manganese atom.[8] This consideration shows that the excited p states

TABLE I. One-electron energies in a.u. for bound $l = 1$ states of the Mn^0 atom generated in two different potentials.

n [a]	ϵ_{np} (in $3p$ potential)	ϵ_{np} (in $4s$ potential)	ϵ_{np} (Clementi [b])
2	−26.071 49	−25.177 31	−24.447 42
3	−2.479 79	−2.824 91	−2.130 67
4	−0.231 05	−0.132 68	
5	−0.066 00	−0.056 05	
6	−0 034 95	−0.031 27	
7	−0.021 76	−0.019 97	
8	−0.014 87	−0.013 86	
9	−0.010 81	−0.010 18	

[a] Principal quantum number.
[b] See Ref. 9.

in $4s$ potential, where $4s \rightarrow 4p$ excitation is important for certain reasons, are more physical and should be used for the calculation. The higher-excited p states are not very sensitive to the two different choices of potential, as seen from the one-electron energies listed in Table I for these states. The results of the individual diagrams in this paper which involve excited p states are presented for basis p states in the $3p$ potential. For comparison, we have also listed in the last column the $2p$ and $3p$ occupied-state energies from Clementi's table.[9] The $3p$ energy in the $3p$ potential is closer to Clementi's $3p$ value, as it should be. The d, f, and g states were generated in the $3d$ potential. The RHF wave functions of Clementi were used for the occupied states to obtain the V^{N-1} potential used in generating the excited states. The radial one-electron equations corresponding to Eq. (5) for different states are given elsewhere,[10] and for economy of space we shall not repeat them here.

C. Diagrams

As was pointed out in Sec. II A the diagrams arising from the expression (7) can be grouped in different orders depending on values of the indices m and n. Owing to the Hermiticity of the operator O, the (m,n) diagram is equal to the (n,m) diagram. The $(0, 0)$ diagram in the present case gives zero contribution, since the zero-order many-particle state is the RHF state of the system, in which the unpaired one-electron states are d states with zero density at the nucleus and the contributions from core s states of opposite spin cancel each other.
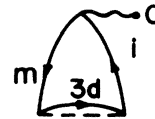

FIG. 1. Exchange-core-polarization diagram for contact interaction in the Mn atom.

The next-order diagram, namely $(0, 1)$, is shown in Fig. 1. It represents the exchange-core-polarization (ECP) effect. Since the operator involved in the spin density, Eq. (13) is a δ function; the excited states i in this diagram should be only s states. The $(1, 1)$ diagrams that make the major contribution are shown in Fig. 2 and the $(0, 2)$ diagrams are shown in Fig. 3. Among these, the diagrams 1(a), 1(b), and 3(a)–3(d) represent one-electron effects. Some of these diagrams can be considered as ladders to the $(0, 1)$ diagram shown in Fig. 1. For example, Fig. 3(a) with $m = n = 3s$ and Fig. 3(b) with $m = 3s$ and $q = 4s$ can be considered as ladders to the diagram in Fig. 1 with $m = 3s$. Similar definitions apply to the ladder diagrams corresponding to $m = 1s$ and $2s$. The diagrams in Figs. 2(a), 2(b), 3(c), and 3(d) and for $m \neq n$ in 3(a) are termed consistency diagrams.

The diagrams in Fig. 2(c)–2(f) and 3(e)–3(h) are the two-electron or correlation diagrams, since at any particular instant of time two electrons remain simultaneously excited. In each of these correlation diagrams, either a $3d^+$ hole state or a $3d^-$ particle state, or both, should be present; otherwise the spin cancellation among the s hole states of opposite spin would make the corresponding diagram vanish. This is understandable since hyperfine effects to any order arise in the first place from the influence of the unpaired $3d$ states.

In Fig. 4 we have shown some of the important diagrams of order higher than second. The diagrams in Figs. 4(a) and 4(b) represent the influence on the ECP diagram in Fig. 1 of the pair correlation of the hole state m with other states. The effect of summing all diagrams obtained from 4(a) and 4(b) by adding pair-correlation vertices to the hole line m to infinite order can be incorporated simply by adding the correlation energy of the
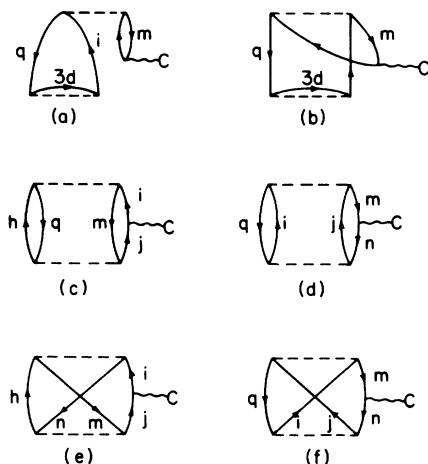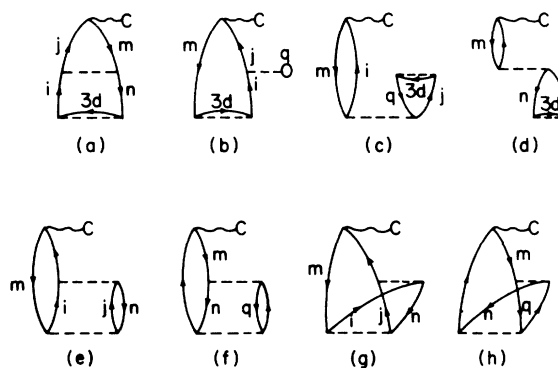

FIG. 3. Major contributing $(0, 2)$ magnetic hyperfine diagrams of the Mn atom.

state with all other states in the energy denominator of the diagram of Fig. 1 as described in earlier literature.[5] In this respect, these diagrams represent their influence of the "dressing" of the hole lines through pair correlation.

The third-order diagrams 4(c) and 4(d) cannot be summed to all orders analytically, as could the dressing diagrams in Figs. 4(a) and 4(b). However, one can use a geometric-series approximation to them using their ratio to the parent diagram in Fig. 1. A similar procedure can be adopted for summing over higher-order consistency diagrams 4(e) by taking the ratio of diagram 3(d) to Fig. 1. We should point out that diagrams 4(a)–4(d) have counterparts where the pair-correlation vertices and bubbles are connected to the particle side of Fig. 1. Other diagrams of third and higher order besides these have been examined and found to be relatively insignificant in magnitude.
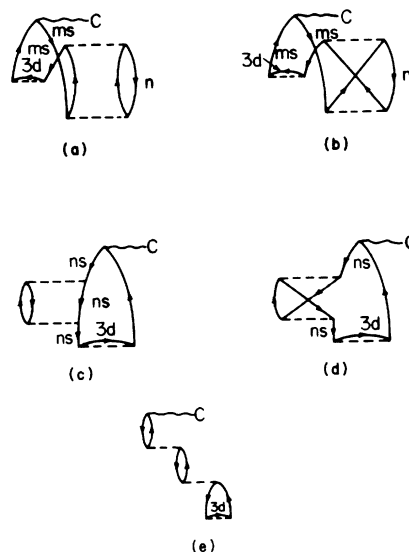

FIG. 2. Major contributing $(1, 1)$ diagrams of the magnetic hyperfine constant for the Mn atom.

FIG. 4. Some important third-order contact diagrams for the Mn atom.

TABLE II. Contributions in MHz from $(0,1)$ contact diagrams of the Mn^0 atom shown in Fig. 1 and comparison with the results by moment-perturbation procedure.

m	Unladdered	Laddered	Moment perturbation [a]
$1s$	0.2	0.2	1.6
$2s$	−273.0	−287.7	−289.1
$3s$	−77.0	−80.1	−70.1
$4s$	215.0	215.0	222.1
Total	−134.8	−152.6	−135.5

[a] Unpublished calculations by D. Ikenberry and T. P. Das.

III. NONRELATIVISTIC VALUES OF DIAGRAMS

In Tables II–IV we have presented the contributions from the diagrams up to second order denoted, as explained before, as $(0,1)$, $(1,1)$ and $(0,2)$. In the present system, because there is no unpaired s electron and the zero-order function of the atom is RHF in nature, the $(0,0)$ diagrams make no contribution. The $(1,1)$ and $(0,2)$ diagrams are rather large in number; for brevity we have listed individually only those diagrams for which the magnitudes are larger than 1 MHz.

The contributions from the $(0,1)$ diagrams shown in Fig. 1, representing the ECP effect, are

TABLE III. Contributions from $(1,1)$ contact diagrams of the Mn^0 atom shown in Figs. 2(a)–2(f).

Diagram	Excitation			Contribution [a] (MHz)
	Consistency			
2(a)	$q=4s^+$	$m=4s^-$		10.1
	$q=2s^+$	$m=2s^-$		−1.5
2(b)	$q=4s^+$	$m=3s^+$		6.5
	$q=4s^+$	$m=2s^+$		3.0
	$q=3p^+$	$m=3s^+$		2.6
	$q=2p^+$	$m=2s^+$		−1.7
Other consistency diagrams				−0.8
Total consistency contribution				18.2
	Correlation			
2(c)	$q=4s$	$m=3d$		5.9
	$q=3p$	$m=3d$		3.9
2(d)	$q=4s$	$m=n=3s^-$		2.3
	$q=3d$	$m=n=4s^-$		2.3
	$q=3d$	$m=4s^-$	$n=3s^-$	2.3
	$q=3d$	$m=n=3s^-$		10.3
	$q=3d$	$m=3s^-$	$n=3s^-$	−1.6
	$q=3d$	$m=3s^-$	$n=2s^-$	−4.2
	$q=3p$	$m=n=3s^-$		19.0
	$q=3p$	$m=3s^-$	$n=2s^-$	−7.2
2(e)		$m=4s$	$n=3d$	3.0
		$m=3d$	$n=3p$	−6.4
2(f)	$q=3d$	$m=n=4s^+$		9.8
	$q=3d$	$m=4s^+$	$n=3s^+$	−2.7
	$q=3d$	$m=n=3s^+$		12.3
	$q=3d$	$m=3s^+$	$n=2s^+$	−5.2
	$q=3d$	$m=n=2s^+$		1.6
	$q=3p$	$m=4s^-$	$n=3s^-$	−2.3
	$q=3p$	$m=n=3s^-$		−13.2
	$q=3p$	$m=3s^-$	$n=2s^-$	8.3
	$q=2p$	$m=n=2s^-$		−2.3
Other correlation diagrams				1.4
Total correlation				37.3
Net $(1,1)$ contribution				55.5

[a] For the sake of brevity, only those diagrams whose magnitudes are greater than 1 MHz are listed.

TABLE IV. Contribution to the magnetic hyperfine constant of Mn^0 from the $(0, 2)$ diagrams shown in Figs. 3(a)–3(h).

Diagram	Excitation			Contribution (MHz)
	Consistency			
3(a)	$m = 3s$	$n = 4s$		8.9
	$m = 3s$	$n = 2s$		−1.3
	$m = 3s$	$n = 3p$		10.9
	$m = 2s$	$n = 4s$		3.1
	$m = 2s$	$n = 3s$		−1.2
	$m = 2s$	$n = 2p$		−12.3
3(c)	$m = 4s^-$	$q = 4s^+$		9.2
	$m = 3s^-$	$q = 3s^+$		−1.3
3(d)	$m = 4s^-$	$n = 4s^+$		19.3
Other consistency				−4.2
Total consistency				31.1
	Correlation			
3(e)	$m = 4s$	$n = 4s$		3.0
	$m = 4s$	$n = 3d$		−15.2
	$m = 4s$	$n = 3p$		−5.6
	$m = 4s$	$n = 3s$		1.6
	$m = 3s$	$n = 4s$		1.0
	$m = 3s$	$n = 3d$		2.0
	$m = 3s$	$n = 3p$		3.0
	$m = 3s$	$n = 2p$		−2.2
	$m = 2s$	$n = 2p$		2.1
3(f)	$q = 4s$	$m = 4s$	$n = 3d$	−5.4
	$q = 4s$	$m = 3s$	$n = 3d$	2.0
	$q = 3p$	$m = 4s$	$n = 3d$	−3.8
	$q = 3p$	$m = 2s$	$n = 3d$	2.0
	$q = 3s$	$m = 3s$	$n = 3d$	−2.7
	$q = 3s$	$m = 2s$	$n = 3d$	1.6
	$q = 2p$	$m = 3s$	$n = 3d$	−1.3
	$q = 2p$	$m = 2s$	$n = 3d$	1.9
3(g)	$m = 4s$	$n = 3d$		−35.3
	$m = 4s$	$n = 3p$		20.5
	$m = 4s$	$n = 3s$		3.0
	$m = 3s$	$n = 3d$		−15.9
	$m = 3s$	$n = 3p$		5.0
	$m = 3s$	$n = 2p$		1.8
	$m = 2s$	$n = 3d$		10.7
	$m = 2s$	$n = 3p$		−1.6
3(h)	$n = 4s$	$m = 4s$	$q = 3d$	−3.9
	$n = 4s$	$m = 3s$	$q = 3d$	−3.2
	$n = 3d$	$m = 4s$	$q = 4s$	−2.1
	$n = 3d$	$m = 4s$	$q = 3p$	2.7
	$n = 3d$	$m = 4s$	$q = 3s$	2.1
	$n = 3d$	$m = 3s$	$q = 4s$	−1.9
	$n = 3d$	$m = 3s$	$q = 3p$	−2.0
	$n = 3d$	$m = 3s$	$q = 3s$	13.0
	$n = 3d$	$m = 2s$	$q = 3p$	−3.9
	$n = 3d$	$m = 2s$	$q = 2s$	−7.0
	$n = 3p$	$m = 4s$	$q = 3d$	3.0
	$n = 3p$	$m = 3s$	$q = 3d$	4.1
	$n = 3p$	$m = 2s$	$q = 3d$	−2.5
	$n = 3p$	$m = 2s$	$q = 2p$	2.2
	$n = 3s$	$m = 4s$	$q = 3d$	3.0

TABLE IV. *(Continued)*

Diagram	Excitation			Contribution (MHz)
3(h)	$n = 3s$	$m = 3s$	$q = 3d$	7.7
	$n = 3s$	$m = 2s$	$q = 3d$	-2.4
	$n = 2p$	$m = 3s$	$q = 3p$	-1.6
	$n = 2s$	$m = 2s$	$q = 3d$	1.7
Other correlation				0.4
Total correlation				-18.4
Net $(0, 2)$ contribution				12.7

listed in Table II. The second column in Table II lists the unladdered values; the third column lists the laddered values involving the diagrams such as 3(a) and 3(b) described in Sec. II. The total contribution from $(0, 1)$ diagrams, including the ladder diagrams, is -152.6 MHz. Comparing the contributions from individual shells of the atom, one can observe first that the magnitudes of the contributions from the $2s$ and $4s$ states are larger than $1s$ and $3s$ diagrams. This difference in the magnitudes of the ECP contribution for various shells can be explained by considering the combined effects of the size of the density at the nucleus for the core electrons and the strength of their exchange with the valence $3d$ electrons. Thus, considering the $1s$ contribution, even though the density at the nucleus for the $1s$ wave function is very large, its overlap with $3d$ is very small, leading to a very small exchange effect. In the case of the $2s$ contribution, the density at the nucleus is quite large; also, the overlap with $3d$ is substantial, thus making the ECP contribution quite substantial.

The explanation of the substantially smaller magnitude of the ECP contribution from the $3s$ state relative to $2s$ requires the consideration of several factors. First, the amplitude of the $3s$ wave function at the nucleus is substantially smaller, so that the response at the nucleus to the exchange polarization effect is weaker. The exchange effect for $3s$ would, however, be expected to be stronger than for $2s$ because of the greater overlap of $3s$ with $3d$. However, the $3s$ orbital has one more node than $2s$ and consequently the exchange matrix elements in Fig. 1 suffer from greater cancellations, in the case of $3s$, from different regions in r, leading to reduction of the exchange effect. In comparing the relative magnitudes of $4s$ and $3s$ contributions, the dominant factor is the substantial larger exchange interaction between the $4s$ and $3d$ as compared to that between $3s$ and $3d$; this more than compen-

sates for the smaller $4s$ amplitude at the nucleus. This substantially larger exchange interaction for the $4s$ case is partly due to the stronger overlap with $3d$ than occurs in the case of $3s$, but, more importantly, there is less cancellation in the exchange matrix element for the $4s$ state from different regions in r, since the exchange with $3d$ occurs mainly at the outer regions of the $4s$ orbital.

The signs of the ECP contributions from individual shells also show interesting trends. Thus, leaving aside the $1s$ shell which essentially makes zero contribution, the other two inner s shells, $2s$ and $3s$, make negative contributions, while the $4s$ shell makes a positive contribution. This trend can be understood by realizing that the $2s$ and $3s$ shells are internal with respect to the $3d$ shell and so have the densities of their parallel-spin electrons diminished at the nucleus by the exchange attraction towards the $3d$ shell. The $4s$ shell, on the other hand, is more external than $3d$, with the exchange now causing an inward movement of parallel-spin $4s$ electrons, leading to enhanced density at the nucleus. This type of behavior was also found in the Fe^0 atom[11] and in other heavier atoms and ions such as in rare-earth systems,[12] where the unpaired shell is external to some of the s shells and internal to others.

Considering next the laddering effect, the results listed in the third column of Table II represent the effect of ladders to all orders obtained from the ratio of the second-order diagrams in Figs. 3(a) and 3(b) to the corresponding parent diagrams in Fig. 1 and using a geometric-series approximation. The laddering contribution from $2s$ has larger absolute magnitude than that from $3s$, but the latter is proportionately larger. This result can be understood by realizing that the perturbations due to the ladder in Figs. 3(a) and 3(b) depend on the deformability of the core states in question, the $3s$ state being stronger in this respect than $2s$. In column 4 of Table II we have

listed the ECP contributions from moment-per-turbation calculations,[13] which are seen to agree quite well with the (0,1) results of LCMBPT listed in column 3 of Table II, in common with a number of other systems where such comparisons have been made.[2,5,13]

In Table III, we have presented the contributions from (1,1) diagrams which are further separated into consistency and correlation contributions. In considering the contributions from Fig. 2(a), the diagrams involving the consistency interaction between $4s$ states can be seen from Table III to be the dominant one. The consistency diagram involving the $3s$ state is less than 1.0 MHz in magnitude and is not shown in Table III. The corresponding diagram involving $2s$ states is somewhat larger in magnitude than the $3s$ diagram but substantially smaller than the $4s$. The sizes of these diagrams depend both on the sizes of the corresponding ECP diagrams in Fig. 1 and the deformability of the s states. Since the $4s$ state is dominant in both these respects, the largest relative magnitude of the $4s$-$4s$ consistency diagram is understandable. Figure 2(b) represents the exchange counterpart of Fig. 2(a) and exists only when $m \neq q$. The relatively larger contributions among diagrams in this class for $q = 4s$ is understandable for the same reasons as in the case of 2(a). However, the contributions from interaction between other states of same principal quantum number, such as $3s$ and $3p$, and between $2s$ and $2p$, is a consequence of the greater overlap between such pairs of states.

The diagrams in Figs. 2(c)–2(f) represent correlation effects; from their values in Table III one can observe that correlation effects among electrons with the same principal quantum number are relatively stronger than those among states of different principal quantum numbers, the exception being the case when $4s$ is involved. This behavior can be understood through some of the reasons discussed for diagrams 2(a) and 2(b). The total consistency contribution from (1,1) diagrams is found to be 18.2 MHz and the total correlation effect is found to be 37.3 MHz, leading to a net (1,1) contribution of 55.5 MHz, which is about 30% of the (0,1) contribution and of opposite sign.

We have listed the contributions from various (0,2) diagrams in Table IV. The various intra-shell and intershell contributions to the consistency and correlation effects have the same features and trends as in the case of the (1,1) diagrams. On combining the consistency and correlation diagrams separately as in the case of (1,1), the net consistency and correlation contributions are found to be 31.1 MHz and −18.4 MHz, respectively, leading to a net (0,2) contribution of 12.1 MHz, which, as in the (1,1) case, has a sign opposite to that of the (0,1) result.

To obtain the net hyperfine constant to second order, we need the contributions from the $1s$ diagrams. The (0,1) contribution for this state has been given in Table I and is rather small. In the (1,1) and (0,2) results presented in Tables III and IV, the $1s$ contribution was not included. From the results in Mn^{+2} and Fe^{+3} ions[14,2] which we have previously studied, the $1s$ contribution was expected to be rather small and it was not felt necessary to study all of the diagrams associated with it. Instead, from the results for Mn^{+2} and Fe^{+3} ions, which are expected to have nearly the same $1s$ contribution as in the Mn^0 atom, the $1s$ contribution was estimated as 4.0 MHz, arising mainly from consistency diagrams.

Including the $1s$ contribution (except for ladder-ing effects to all orders for (0,1) diagrams discussed earlier), the net result of our calculation up to second order is −80.4 MHz, which is composed of −99.3 MHz from one-electron effects and 18.9 MHz from two-electron effects. The one-electron effects are a combination of ECP and consistency contributions, while the two-electron effects represent correlation contributions. These results are tabulated in Table V. It should be noted that the two-electron effects in the present case seem to have a fairly substantial ratio (about 18%) as compared to the one-electron effects, which is a higher ratio than in the case of Mn^{+2} and Fe^{+3} ions.[2,14] This larger ratio in the case of the Mn^0 atom is, however, a consequence of the smaller value of the ECP contribution arising from the cancellation between the net effect of $2s$ and $3s$ and the $4s$ contributions, as discussed earlier. The ratio of the correlation contribution to the consistency part of the one-electron effect is comparable for the Mn^0 atom and Mn^{+2} and Fe^{+3}

TABLE V. List of nonrelativistic contributions to the hyperfine constant (in MHz) of the Mn^0 atom, including up to second order in electron-electron interaction.

| (0,1) ECP | (1,1) | | (0,2) | | Net consistency | Net correlation | Total |
	Consistency	Correlation	Consistency	Correlation			
−152.6	20.2 [a]	37.3	33.1 [a]	−18.4	53.5	18.9	−80.4

[a] These results include consistency effects of the $1s$ electron which are not tabulated in Tables III and IV.

ions, although the correlation contribution is substantially larger for the Mn^0 atom. The latter feature is a consequence of the presence in the Mn^0 atom of the diffuse $4s$ shell, which can be polarized substantially in the correlation process involving its pair interaction with other electrons.

Beyond second order the diagrams are very large in number. Therefore in studying higher-order diagrams a selection was made of those diagrams which could be related to the sizable first- and second-order diagrams. Thus in Figs. 4(a)–4(e) we have shown some third-order diagrams which are related to the (0, 1) core-polarization diagrams by the addition of two $1/r_{12}$ vertices. Of these diagrams, 4(a) and 4(b) refer to the dressing effect on the hole lines due to their pair correlation with other electrons. Thus in Fig. 4(a) the hole line $4s$, which is being exchange core polarized by $3d$, also interacts through pair correlation with another hole state n, and 4(b) is its exchange counterpart. The influence of these pair-correlation effects can be calculated to all orders by adding the correlation energy of the mth hole state with all other nth hole states to the energy denominator of the ECP diagram of Fig. 1 of the mth hole state. The influence of this dressing depends on the ratio of the pair-correlation energy to the one-electron energy of the hole state concerned, and since the hole states from $1s$ to $3s$ have small correlation energies, it is the $4s$ hole state which undergoes significant correction due to the dressing. The net pair-correlation energy of $4s$, with the other $4s$ state and with all electrons with principal quantum number 3, is -0.0556 a.u., the major part coming from $4s$-$4s$ and $4s$-$3d$ correlation effects. This number is an appreciable fraction of the $4s$ one-electron energy of -0.2451 a.u., and hence significantly influences the energy denominator in the ECP diagram (Fig. 1) for the $4s$ state. The result of this is represented by the dressing diagrams [Figs. 4(a) and 4(b)], which contribute -24.5 MHz for the $4s$ state. The corresponding contributions for the other core states are rather small. The diagrams in Figs. 4(c) and 4(d) are a few ones typical of the whole set of diagrams one can get by joining the $1/r_{12}$ interaction lines to only hole or only particle lines or partially to hole and partially to particle lines and the corresponding exchange counterparts. The total contribution from these diagrams, after making a geometric-series approximation, is 5.6 MHz, the major contribution coming from $4s$-$4s$ correlation. The diagram in Fig. 4(e) is the higher-order counterpart of 3(d); we have evaluated the contribution from this and higher orders by making a geometric-series approximation utilizing the ratio of Fig. 3(d) to Fig.

1. The contribution from this series of diagrams is 8.5 MHz. Thus the net contribution of the third-order diagrams in Fig. 4 and their higher-order counterparts as included by the geometric-series approximation is then -10.4 MHz. On combining this with our second-order result of -80.4 MHz, we get -90.8 MHz. Therefore the net result from nonrelativistic theory is -90.8 MHz. We ascribe to this an error limit of ± 3.0 MHz. This error limit has been estimated from consideration of effects of higher-order diagrams that have not been included, possible errors associated with geometric-series approximation, neglect of excitations of higher-angular-momentum states than g, and, of course, the limit of computational accuracy. This result is to be compared with the experimental value of 72.422 ± 0.002 MHz.[1] Our net theoretical nonrelativistic result of -90.8 ± 3.0 MHz is thus about 18.4 MHz larger than the experimental value. If, considering the relativistic effects in hydrogenic or the alkali atoms,[3] because of the increase in the density of the electrons at the nucleus one made the simple assumption that the relativistic effect on all diagrams in Mn^0 would be an increase in density owing to contraction of the orbitals, then relativistic effects would be expected only to make the result go further away from experiment. However, as we shall see in Sec. IV, which deals with actual calculation of the (0, 1) diagrams starting with Dirac-Hartree-Fock zero-order wave functions, one cannot expect that the only effect of relativistic corrections on different diagrams is to increase their magnitudes. In fact, we shall see that there can even be alterations in sign of the relativistic corrections, which are connected with the influence of relativistic effects on the radial characters of the paired orbitals and their corresponding influence on both the exchange interaction with the unpaired $3d$ shell and their densities at the nucleus.

IV. RELATIVISTIC CALCULATION OF (0,1) DIAGRAMS

In attempting to explain the difference of 18.4 MHz between the nonrelativistic theoretical result and experimental data as mentioned in Sec. III, we have analyzed the influence of relativistic effects. The procedure for calculation of the hyperfine constant of a large atom like Mn^0 in a complete relativistic many-body formalism is difficult to formulate. The main difficulty lies in the fact that one has to use the jm scheme in relativistic theory. Nonrelativistically the Mn^0 atom has a single determinant to start with, since it is half filled, which makes the handling of the many-body perturbation theory relatively simple. In the jm scheme,

the ground state is no longer a single determinant but is made up of many determinants. As a first step towards a practical way of handling the entire many-body problem we have formulated the relativistic theory in order to be able to evaluate the contributions of the (0, 1) diagrams after obtaining a complete set of relativistic basis states. This was done keeping in mind first that the major contribution to the hyperfine constant A_c in nonrelativistic theory comes from these diagrams and second that their evaluation involves only s excited states. In the following subsections we describe the theoretical procedure used to evaluate these diagrams.

A. Description of the procedure

First we formulate the ground state (^6S) of the Mn^0 atom in the jm scheme according to the procedure prescribed by Sandars and Beck.[15] This can be done by expressing the $3d$ up spin orbitals by jm orbitals which in turn are then replaced by Dirac four-component spinors.[16] As an example, a $3d$ orbital of the Mn^0 atom with $m_l = -2$ and $m_s = +\frac{1}{2}$ can be expressed in the jm scheme as

$$-2^+ = (1/\sqrt{5})|\tfrac{5}{2} - \tfrac{3}{2}\rangle - (2/\sqrt{5})|\tfrac{3}{2} - \tfrac{3}{2}\rangle, \tag{14}$$

where the kets are in jm notation. Another example (given for the 1^+ state) is

$$1^+ = (2/\sqrt{5})|\tfrac{5}{2}\tfrac{3}{2}\rangle - (1/\sqrt{5})|\tfrac{3}{2}\tfrac{3}{2}\rangle. \tag{15}$$

Similar expressions can be obtained for the other $3d$ orbitals; at the end all kets are replaced by Dirac spinors.[17] After making the choice of the ground state, the derivation of the Dirac-Fock equations for the occupied states follows the same pattern as in the nonrelativistic case.[18] Details of this derivation of the Dirac-Fock equations are given elsewhere.[19]

In order to calculate the excited basis states it is necessary to make a choice of the potential. In the present work, we have chosen this potential in a way analogous to the nonrelativistic formulation, that is, utilizing a V^{N-1} potential, but in the relativistic formulation a j excited state is obtained from a j core state in place of an l state from an l' core state in the nonrelativistic case. As pointed out earlier, since our present motivation is to evaluate the (0, 1) diagrams, we need only the s excited states. We obtain these by creating the excited $s_{1/2}$ states in a V^{N-1} potential with a $4s_{1/2}$ electron missing. We have created both the bound and continuum states in the basis by utilizing a numerical procedure developed by Coulthard[20] and revised by one of us (J. A.). We have created four excited bound states and twelve continuum states. For the sake of comparison of the bound-state energies and spin densities at the nucleus for rela-

tivistic and nonrelativistic cases we have listed these quantities in Tables VI and VII. In Table VI we have listed the energy values of different excited states in the V^{N-1} potential. It can be observed that for the low-lying states the energies are different, being deeper in the relativistic case, as it should be. However, for higher n values the difference becomes smaller because the peaks of the orbitals are further away from the nucleus and so the relativistic effects become less important.

In order to compare the matrix elements in the relativistic and nonrelativistic formalisms we first compare the entities ρ^{NR} of nonrelativistic case with the expression

$$\rho^{rel} = \frac{1}{2\pi\alpha}\left(\int_0^\infty \frac{P_n Q_{n'}}{r^2}\,dr + \int_0^\infty \frac{P_{n'} Q_n}{r^2}\,dr\right) \tag{16}$$

between states n and n' of the relativistic formalism. In expression (16) P equals r times the large component of the radial functions and Q equals r times the small component, in relativistic theory, in atomic units, and α is the fine-structure constant. ρ^{rel} reduces to ρ^{NR} in the nonrelativistic limit.[4] We also compare the nonrelativistic radial integrals

$$I^{NR} = \langle P_n P_{3d} | 1/r_{12} | P_{3d} P_{n'} \rangle$$

with the relativistic counterpart

$$I^{rel} = \langle P_n P_{3d^+} | 1/r_{12} | P_{3d^+} P_{n'} \rangle + \langle Q_n Q_{3d^+} | 1/r_{12} | Q_{3d^+} Q_{n'} \rangle. \tag{17}$$

In expression (17) $3d^+$ means that we use the $j = \frac{5}{2}$ states of $3d$ in relativistic notation. The difference between the (0, 1) result using $3d^+$ and $3d^-$ wave functions was found to be negligible for the Mn^0 atom. However, the situation could be different in other systems. In Table VII we have compared ρ^{rel} and I^{rel} with their nonrelativistic counterparts ρ^{NR} and I^{NR}, respectively, and it is seen that the magnitude of ρ^{rel} is always larger than that of ρ^{NR},

TABLE VI. Comparison of nonrelativistic and relativistic one-electron s bound-state energies. The energies are expressed in a.u. (e^2/a_0).

n	Nonrelativistic energy	Relativistic energy
1		−242.968 00
2	−29.472 52	−29.900 16
3	−4.157 95	−4.226 17
4	−0.245 06	−0.250 71
5	−0.080 29	−0.080 74
6	−0.040 63	−0.040 78
7	−0.024 55	−0.024 62
8	−0.016 44	−0.016 47

TABLE VII. Comparison of ρ and I integrals (in a_B^{-3}) as defined by Eqs. (13b)–(15) between states n and n'. The superscripts NR and rel stand for the nonrelativistic and relativistic integrals.

n	n'	ρ^{NR}	ρ^{rel}	I^{NR}	I^{rel}
2	5	13.6458	14.6444	−0.0054	−0.0052
	6	8.1285	8.7099	−0.0032	−0.0031
	7	5.5601	5.9532	−0.0022	−0.0021
	8	4.1128	4.4147	−0.0016	−0.0016
3	5	5.0127	5.3861	0.0020	0.0014
	6	2.9860	3.2034	0.0012	0.0008
	7	2.0425	2.1895	0.0008	0.0005
	8	1.5108	1.6237	0.0006	0.0004
4	5	1.0877	1.1755	0.0115	0.0120
	6	0.6479	0.6991	0.0067	0.0070
	7	0.4432	0.4778	0.0045	0.0047
	8	0.3278	0.3544	0.0033	0.0034

as expected. For I^{rel} and I^{NR} the differences are less pronounced than for ρ^{rel} and ρ^{NR}.

B. Evaluation of (0,1) diagrams using the relativistic basis set

We next describe the evaluation and results of (0, 1) diagrams with the relativistic basis set we have generated. After obtaining the integrals ρ^{rel} and I^{rel} as listed in Table VII, the evaluation of the (0, 1) relativistic diagrams is relatively straightforward. In Table VIII, we compare the contributions from (0, 1) diagrams evaluated both relativistically and nonrelativistically, including laddering effects. A very interesting feature can be observed from Table VIII. The relativistic effect is seen to increase the magnitude of the 4s contribution, whereas it decreases the 2s contribution. The 3s contribution increases slightly in magnitude. This behavior of the influences of the relativistic effect on different shells can be understood by examining the radial characteristics of the nonrelativistic 2s, 3s, 4s, and 3d wave functions as plotted in Fig. 5. Relativistic effects mainly lead to a contraction of the s orbitals, while the 3d orbital is not subject to as much rela-

TABLE VIII. Comparison of values (in MHz) of relativistic and nonrelativistic ECP diagrams including laddering effects.

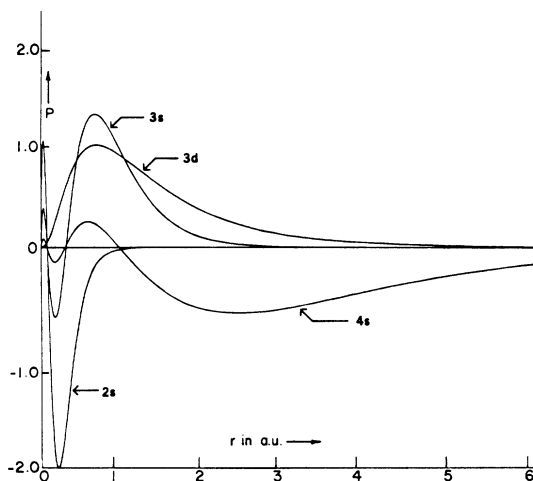| m	Relativistic	Nonrelativistic
1s	1.8	0.2
2s	−281.7	−287.7
3s	−90.7	−80.1
4s	227.0	215.0
Total	−143.6	−152.6

FIG. 5. Plot of the Mn^0 ground-state 2s, 3s, 4s, and 3d nonrelativistic orbitals.

tivistic effect since it damps out as r^3 near the nucleus, which makes its amplitude near the nucleus very small. Because of the contraction of the 4s orbital, not only does its density at the nucleus increase but also its exchange interaction with the 3d orbital increases, since the 4s orbital moves closer to the 3d orbital, the latter remaining pretty much stationary after the relativistic effect. This effect can be seen pictorially in Fig. 6. The 3s orbital, on the other hand, while it has an increase in its density near the nucleus because of the relativistic effect, has its exchange with the 3d state reduced because of its moving away from the 3d orbital, as explained in Fig. 6. Thus in the case of the 3s shells the increase in density at the nucleus counterbalances the decrease in its exchange with 3d, leading to a substantially smaller net change of the (0, 1) diagram relative to the 4s case. In the case of 2s, however, the substantial
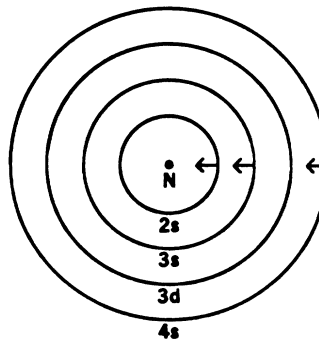

FIG. 6. Influence of relativistic changes of orbitals on exchange interaction and contact density. N is the position of the nucleus. The arrows show the contraction of orbitals due to relativistic effect.

TABLE IX. Summary of various contributions to the hyperfine constant (in MHz) in the Mn^0 atom.

Contribution from ECP	-152.6
Consistency up to second order	53.3
Correlation up to second order	18.9
Contribution from third and higher orders	-10.4
Relativistic correction to ECP	9.0
Relativistic corrections to consistency and correlation	12.0
Casimir effect	-4.3
Net result	-74.1 ± 3.0
Experiment [a]	-72.422 ± 0.0002

[a] See Ref. 1.

increase of its density near the nucleus cannot be counterbalanced by the decrease in exchange with the $3d$ state, as the $2s$ orbital moves away from the $3d$, and in fact we see a decrease in the magnitude of the $(0,1)$ diagram shown in Fig. 1 with $m = 2s$. In effect this explanation of the trend draws on the similar considerations of the relative radial characters of the $2s-4s$ orbitals and their locations relative to the $3d$ orbital, as was the case when we dealt with, in Sec. III, the signs of the contributions from nonrelativistic $(0,1)$ diagrams. From a combination of these relativistic effects on the ECP contributions from different paired s states we now get a net increase of 9.0 MHz relative to the nonrelativistic ECP effect from the laddered $(0,1)$ diagrams. This relativistic contribution reduces the magnitude of the theoretical result for A_c to -81.8 ± 3.0 MHz, reducing the gap with the experimental value.

The main relativistic effect on the $(0,1)$ diagrams was found to arise from changes in the matrix elements involving the orbitals, rather than the changes in the one-electron energies occurring in the denominator. Considering these changes in the matrix elements, we have estimated the relativistic corrections to the $(1,1)$ and $(0,2)$ diagrams which make sizable contributions in nonrelativistic theory, and we have arrived at a total relativistic correction of 12.0 MHz from these diagrams. Combining this we get a net contribution from various orders including the relativistic effect of -69.8 ± 3.0 MHz.

In obtaining the net theoretical result to compare with experiment, it is necessary to include two additional contributions. These are the BDLSC (breakdown of LS coupling) effect and the Casimir effect, as discussed by Sandars and Beck.[15] We found the former effect to be negligible, whereas the latter, evaluated with our relativistic d functions, is[21] -4.3 MHz. Our final theoretical result, including, in principle, all orders of correlation and relativistic effects, is -74.1 ± 3.0 MHz.

To present at a glance the relative importance of all of the physical effects that have been included in our present analysis, we have listed their net contributions in Table IX. It is clear from this table that in order to obtain quantitative agreement with experiment within the range of accuracy of our work, each of the effects (ECP, consistency, correlation, and relativistic effects) must be carefully evaluated and incorporated.

V. CONCLUSION

The conclusions of our present work on the manganese atom can be summarized as follows: The net contribution from the $(0,1)$ diagrams, representing the ECP effect, is substantially different from experiment, in contrast to the cases[2,14] of Mn^{+2} and Fe^{+3} ions. However, by a careful analysis of correlation effects, relativistic effects, and their interplay, one is able to obtain very good agreement with experiment for the manganese atom. The relativistic effect on the ECP diagrams has two interesting features. First, the relativistic corrections to the ECP diagrams for the $2s$, $3s$, and $4s$ shells are of comparable magnitude and, second, there is a remarkable change in sign in the relativistic correction for the $4s$ state, as compared to the $3s$ and $2s$ states. We have suggested physical explanations for these features in Sec. IV. We expect similar trends for the relativistic corrections to $(0,1)$ diagrams in other transition-metal atoms. It would be useful to verify this conclusion by more calculations in these systems and also to study the trend in the variations in relativistic effects on correlation diagrams over the transition-metal-atom series.

We therefore hope that the present investigations of many-body and relativistic effects in the manganese atom will stimulate further efforts in Dirac—many-body theory in other transition-metal atoms in addition to efforts already underway in unrestricted Dirac-Hartree-Fock theory.[22]

*Work at State University of New York at Albany is supported by the National Science Foundation.

†Present address: Laboratory of Solid State Physics, Materials Science Center, University of Groningen, The Netherlands.

[1]S. J. Davis, J. J. Wright, and L. C. Balling, Phys. Rev. A 3, 1220 (1971); G. K. Woodgate and J. S. Martin, Proc. Phys. Soc. Lond. A 70, 485 (1957).

[2]S. N. Ray, Taesul Lee, and T. P. Das, Phys. Rev. B 8, 5291 (1973).

[3]H. B. G. Casimir, *Interaction Between Atomic Nuclei and Electrons* (Freeman, San Francisco, 1963).

[4]L. Tterlikkis, S. D. Mahanti, and T. P. Das, Phys. Rev. 176, 10 (1968).

[5]S. N. Ray, Taesul Lee, and T. P. Das, Phys. Rev. A 7, 1469 (1973); T. Lee, N. C. Dutta, and T. P. Das, Phys. Rev. A 1, 995 (1970); H. P. Kelly, Phys. Rev. 173, 142 (1968).

[6]J. Goldstone, Proc. R. Soc. A 239, 267 (1957); K. A. Brueckner, Phys. Rev. 97, 1353 (1955); 100, 36 (1955).

[7]B. N. Taylor, W. H. Parker, and D. N. Largenberg, Rev. Mod. Phys. 41, 375 (1969); *Nuclear Magnetic Resonance Tables*, Fifth ed. (Varian, New York, 1965).

[8]C. E. Moore, *Atomic Energy Levels*, Vol. II, Nat. Bur. Stand. Circ. No. 467 (U.S. GPO Washington, D.C., 1952).

[9]E. Clementi, IBM J. Res. Dev. 9, 2 (1965).

[10]S. N. Ray, Ph.D. thesis (State University of New York at Albany, 1975) (unpublished).

[11]H. Kelly and A. Ron, Phys. Rev. A 2, 1261 (1970).

[12]D. Ikenberry, T. P. Das, and J. B. Mann, Phys. Rev. A 4, 2188 (1971).

[13]G. D. Gaspari, W.-M. Shyu, and T. P. Das, Phys. Rev. 134, A852 (1964).

[14]D. Ikenberry, N. C. Dutta, and T. P. Das, AIP Conf. Proc. 5, 805 (1972).

[15]P. G. H. Sandars and J. Beck, Proc. R. Soc. A 289, 97 (1965).

[16]See, for example, L. I. Schiff, *Quantum Mechanics*, third ed. (McGraw-Hill, New York, 1968).

[17]J. Andriessen (internal report, Laboratorium voor Technische Natuurkunde, Lorentzweg 1, Delft, Netherlands, 1974) (unpublished).

[18]I. P. Grant, Proc. R. Soc. A 262, 555 (1961).

[19]J. Andriessen and D. van Ormondt, J. Phys. B 8, 1993 (1975).

[20]M. A. Coulthard, J. Phys. B 6, 2224 (1973).

[21]D. van Ormondt (private communication).

[22]J. V. Mallow, A. J. Freeman, and J. P. Desclaux, Bull. Am. Phys. Soc. 20, 291 (1975).